High-resolution mapping of urban air quality with heterogeneous observations: a new methodology and its application to Amsterdam

Bas Mijling[1]

[1]Royal Netherlands Meteorological Institute (KNMI), Postbus 201, 3730 AE, De Bilt, The Netherlands

5   *Correspondence to*: Bas Mijling (mijling@knmi.nl)

Abstract. In many cities around the world people are exposed to elevated levels of air pollution. Often local air quality is not well known due to the sparseness of official monitoring networks, or unrealistic assumptions being made in urban air quality models. Low-cost sensor technology, which has become available in recent years, has the potential to provide complementary information. Unfortunately, an integrated interpretation of urban air pollution based on different sources is not straightforward

10   because of the localized nature of air pollution, and the large uncertainties associated with measurements of low-cost sensors. In this study, we present a practical approach to producing high spatio-temporal resolution maps of urban air pollution capable of assimilating air quality data from heterogeneous data streams. It offers a two-step solution: (1) building a versatile air quality model, driven by an open source atmospheric dispersion model and emission proxies from open data sources, and (2) a practical spatial interpolation scheme, capable of assimilating observations with different accuracies.

15   The methodology, called Retina, has been applied and evaluated for nitrogen dioxide (NO_2) in Amsterdam, the Netherlands, during the summer of 2016. The assimilation of reference measurements results in hourly maps with a typical accuracy of 39% within 2 km of an observation location, and 53% at larger distances. When low-cost measurements of the Urban AirQ campaign are included, the maps reveal more detailed concentration patterns in areas which are undersampled by the official network. During the summer holiday period, NO_2 concentrations drop about 10% due to reduced urban activity. The reduction is less in

20   the historic city center, while strongest reductions are found around the access ways to the tunnel connecting the northern and the southern part of the city, which was closed for maintenance. The changing concentration patterns indicate how traffic flow is redirected to other main roads.

Overall, we show that Retina can be applied for an enhanced understanding of reference measurements, and as a framework to integrate low-cost measurements next to reference measurements in order to get better localized information in urban areas.

25   ## 1 Introduction

Due to growing urbanization in the last decades, more than half of the world's population lives in cities nowadays. Dense traffic and other human activity, in combination with unfavourable meteorological conditions, often cause unhealthy air pollution concentrations. Over 80% of the urban dwellers are forced to breathe air which does not meet the standards of the World Health Organization (WHO, 2016). In 2015, an estimated 4.5 million people died prematurely from diseases attributed

30 to ambient air pollution (Lelieveld et al., 2018). Good monitoring is important to better understand the local dynamics of air pollution, to identify hot spots, and to improve the ability to anticipate events. This is especially relevant for nitrogen dioxide (NO_2) concentrations, which can vary considerably from street to street. NO_2 is, apart from being a toxic gas on its own, an important precursor of particulate matter, ozone, and other regional air pollutants. Observations from a single location are not necessarily representative for a larger area. Unfortunately, urban air quality reference networks are usually sparse or even

35 absent due to their high installation and maintenance costs. New low-cost sensor technology, available for several years now, has the potential to extend an official monitoring network significantly, even though the current generation of sensors have significant lower accuracy (WMO, 2018).

However, adding value to the measurements (either official or unofficial), apart from publishing the data as dots on a map, is not straightforward. Our aim is to make better use of the existing measurement networks to get the best description of hourly

40 urban air quality, and to create value from low-cost measurements towards a Level 4 product, according to the classification proposed by Schneider et al. (2019)

To obtain high-resolution information, a very sparse observation network needs to be accompanied by a valid high-resolution air quality model, whereas a very dense network can do with simple spatial interpolations. The situation in most large cities is somewhere in between. There is often a reasonably large reference network present (10+ stations), sometimes complemented

45 with an experimental network of low-cost AQ sensors. Assumptions about underlying unresolved structures in the concentration field are still needed, but this can be done with a simplified air quality model, using the available measurements to correct simulation biases where needed.

A popular approach in detailed mapping of air quality is land use regression modelling (LURM), see e.g. Beelen et al. (2013). LURM uses multiple linear regression to couple a broad variety of predictor variables (geospatial information such as traffic,

50 population, altitude, land use classes) to the observed concentrations. It is typically used in exposure studies, which target long integration intervals by definition. Problems of over-fitting might arise when too many predictor variables are used. Alternatively, Denby (2015) advocates the use of less proxy data, and a model based on more physical principles. In his approach, the emission proxies are first (quasi) dispersed with a parameterized inverse distance function, before being coupled to observed concentrations in a regression analysis.

55 Mapping of air pollution for short time scales is challenging. Only a few scientific studies are published aiming at assimilation of near-real time observations in hourly urban concentration maps. Schneider et al. (2017) use Universal Kriging to combine hourly NO_2 observations of 24 low-cost sensors in Oslo, Norway, with a time-invariant basemap. The basemap is created from a yearly average concentration field calculated with an Eulerian/Lagrangian dispersion model on a 1 km grid, downscaled to 100 m resolution. Averaged over reference locations, their study shows that hourly values compare well with official values,

60 showing the potential of low-cost sensor data for complementary air quality information at these time scales.

In this paper, we present a more advanced yet practical approach to map hourly air pollutant concentrations, named Retina. Its main system design considerations are:
- Observation driven

- Able to assimilate observations of different accuracy
65
- Potential near-real time application
- Versatile / portable to other domains
- Based on open data
- Reasonable computer power

Retina uses a two-stage approach. It runs an urban air quality model to account for hourly variability in meteorological
70 conditions (described in Section 2) which is dynamically calibrated with recent measurements (Section 3). In the second stage
it assimilates current measurements using statistical interpolation (Section 4). Section 5 presents the validation of the system,
while Section 6 shows the added value when assimilating additional low-cost sensor measurements. Section 7 and 8 are
reserved for discussion, conclusion and outlook.

The method is applied to Amsterdam, a city like many where NO_2 emissions are dominated by transport and residential
75 emissions and where local exceedances of limit values are regularly observed. The methodology is flexible enough to be
applied to other cities, mainly because it is relatively easy to implement the urban model for a new domain.

2 Setting up a versatile urban air quality model

Amsterdam is the most populous city in the Netherlands, with an estimated population of 863,000. Located at 52°22′N 4°54′E,
it has a maritime climate with cool summers and moderate winters. Concentrations of NO_2 within the city vary considerably,
80 being partly produced locally and partly transported from outside the city. Measurements of 2016 show that, compared with
regional background values from the CAMS ensemble (see Section 2.2.3), urban background concentrations are on average
around 50% higher, while at road sides NO_2 concentrations are about 100% higher.

One of the largest unknowns when modelling urban air quality is a detailed, up-to-date emission inventory capable of
describing the local contribution. For cities such as Amsterdam the local emissions are dominated by the transport and
85 residential sector. This is confirmed by the EDGAR HTAP v2 emission inventory (Janssens-Maenhout et al., 2013), which
estimates the contribution of NO_X emissions in a 20×33 km^2 (0.3 degree) area around the center being 62%, 20%, 12%, and
6% for the sectors transport, residential, energy, industry respectively. Especially the contribution of road transport is relevant,
as its emissions are close to the ground in densely populated areas. We will use traffic information and population density as
proxies for urban emission (see Section 2.2.1 and 2.2.2).
90 In contrast to the regional atmosphere, the urban atmosphere is more dominated by dispersion processes, while many chemical
reactions are less important due to a relatively short residence time (Harrison, 2018). For the dispersion of the emission sources,
we use the open source steady-state plume model AERMOD (Cimorelli et al., 2004), developed by the American
Meteorological Society (AMS) and United States Environmental Protection Agency (EPA). Based on the emission inventory
and meteorology (see Section 2.2.4), AERMOD calculates hourly concentrations of air pollutants. The concentration
95 distribution of an emission source is assumed to be Gaussian both horizontally as vertically when boundary layer conditions
are stable. In a convective boundary layer, the vertical distribution is described by a bi-Gaussian probability density function.

2.1 AERMOD simulation settings

We use AERMOD version 16216r with simulation settings summarized in Table 1, operating on a rectangular domain of 18 ×
22 km^2 covering the municipality of Amsterdam for the most part. All coordinates are reprojected to a local equidistant
coordinate system with the city center as projection center. Instead of using a regular grid, we use a road-following grid
(Lefebre et al., 2011). This reduces the number of receptor points, while maintaining accurate description of strong gradients
found close to roads. Grid points are defined at 25 and 50 m distances perpendicular to roads, and at parallel distances of 75
and 125 m respectively. The open spaces between these grid points are filled with a regular grid at 125 m resolution. Roads
are modelled as line sources, while residential emissions are described as area sources. The dispersion is calculated for NO_X
to avoid a detailed analysis of the rapid cycling between its constituents NO and NO_2. Afterwards, an NO_2/NO_X ratio is applied,
depending on the available ozone (O_3), see Section 2.1.1.

Memory usage of AERMOD for the Amsterdam domain is proportional to the total number of emission source elements (here
17,069 road fragments and 12,182 residential squares) and the number of receptor points in the road-following grid (here
42,128). The calculation time for a single concentration field is around 10 minutes, but can be reduced to a fraction of this by
parallelizing the code.

2.1.1 Ozone chemistry and lifetime

Primary emissions of NO_2 (e.g. directly from the tailpipe) are only 5-10% of the total emitted NO_X (Sokhi et al., 2007). At
short time scales, secondary NO_2 is formed by oxidation of NO with O_3, while this reaction is counterbalanced by photolysis
converting NO_2 to NO. The reaction rate of the first reaction is temperature dependent, while the latter depends on the available
sunlight. The NO_2/NO_X ratio has therefore an intricate dependence on temperature, radiation, and the proximity to the source
(i.e. the travel time of the air mass since emission).

A practical approach to estimate this ratio is the Ozone Limited Method (OLM), as described in EPA (2015). The method uses
ambient O_3 to determine how much NO is converted to NO_2. The dispersed (locally produced) NO_X concentration is divided
into two components: the primary emitted NO_2 (here assumed to be 10%), and the remaining NO_X which is assumed to be all
NO available for reaction with ambient O_3: $NO+O_3 \rightarrow NO_2+O_2$. If the mixing ratio of ozone (O_3) is larger than the 90% of
(NO_X), than all NO is converted to NO_2. Otherwise, the amount of NO converted is equal to the available O_3, i.e. (NO_2) =
$0.1(NO_X) + (O_3)$. The reaction is assumed to be instantaneous and irreversible. The resulting NO_2 concentration is added to
the NO_2 background concentration.

Removal processes of NO_X are modeled with an exponential decay. The chemical lifetime is in the order of a few hours. Liu
et al. (2016) find NO_X lifetimes in a range from 1.8 to 7.5 h using satellite observations over cities in China and the USA.
Given the size of our domain and average wind speeds, its exact value is not of great importance. Based on regression results,
we choose a practical value of 2 hour.

2.2 Simulation input data

The dispersion simulation is driven by input data regarding emissions, background concentrations, and meteorology, listed in
130   Table 2. All data, except for the traffic counts of inner city traffic, are taken from open data portals. The emission proxies are
mapped in Fig. 1.

2.2.1 Traffic emissions

Road location data and road type definition data are taken from OpenStreetMap (OSM, 2017), which is a crowd-source project
to create a free editable map of the world. We separate urban roads (labeled in OSM as "primary", "secondary", and "tertiary")
135   and highways (labeled as "motorway" and "trunk"), as they have a distinct traffic pulse, fleet composition, and driving
conditions. Road segments labeled as "tunnel" are not taken into account.

When the traffic flow q (in vehicles per hour) is known, the emission rate E for a road segment l can be written as

$$E = \alpha_{\text{veh}} q l \tag{1}$$

with emission factor α_{veh} representing the (unknown) NO_X emission per unit length per vehicle. Hourly traffic flow data is
140   taken from 29 representative highway locations from the National Data Warehouse for Traffic Information (NDW, 2019),
which contains both real-time and historic traffic data. For the urban traffic flow we use data from 24 inductive loop counters
provided by the traffic research department of Amsterdam municipality. Due to its large numbers, traffic flow is relatively
well predictable, especially when lower volumes during holiday periods and occasional road closures are neglected. For each
location we construct a traffic "climatology" parametrized by hour and weekday, based on hourly data of 2016, see Fig. 2.
145   Traffic counts correlate strongly between different highway locations, all showing a strong commuting and weekend effect.
Urban traffic typically shows, apart from lower volumes, less reduction between morning and evening rush hours, a less
pronounced weekend effect, and higher traffic intensities on Friday and Saturday night.

For locations $\mathbf{x}$ between the counting locations $\mathbf{x}_i$ the traffic flow $q(\mathbf{x})$ is spatially interpolated by inverse distance weighting
(IDW):

$$150 \quad q(\mathbf{x}) = \begin{cases} \frac{\sum_i w_i(\mathbf{x}) q_i}{\sum_i w_i(\mathbf{x})}, & \text{if } d(\mathbf{x}, \mathbf{x}_i) \neq 0 \text{ for all } i \\ q_i, & \text{if } d(\mathbf{x}, \mathbf{x}_i) = 0 \text{ for some } i \end{cases} \tag{2}$$

in which the weighting factors w_i depend on the distance d between $\mathbf{x}$ and the counting location $\mathbf{x}_i$:

$$w_i = \frac{1}{d(\mathbf{x}, \mathbf{x}_i)^2} \tag{3}$$

2.2.2 Population data

Population density is considered to be a good proxy for residential emissions, e.g. from cooking and heating. Here we take
155   data from the gridded population database of 2014, compiled by the national Central Bureau for Statistics (CBS, 2019) at a
100 m resolution. Each grid cell is offered to the dispersion model as a separate area source. To reflect the observation that

residential emissions per capita are less when people are living closer to each other (Makido et al., 2012), the emission fluxes are taken proportional to the square root of the population density p:

$$E = \alpha_{\mathrm{pop}}\sqrt{p} \tag{4}$$

2.2.3 Background concentrations

As AERMOD only describes the local contribution to air pollution, we add background concentrations which are taken from the Copernicus Atmosphere Monitoring Service (CAMS) European air quality ensemble (Marécal et al., 2015). The CAMS ensemble consists of 7 regional models producing hourly air quality and atmospheric composition forecasts on a 0.1×0.1 degree resolution. The analysis of the ensemble is based on the assimilation of 1-day old observations provided by the European Environment Agency (EEA). Each model has its own data assimilation system.

In the CAMS product the local contributions are already present. To get a better estimate for regional background concentrations avoiding double counts, we take the lowest concentration found in a 0.3×0.3 degree area around the city for NO_2, and the mean concentration found in this area for O_3.

2.2.4 Meteorological data

The dispersion of air pollution is strongly governed by local meteorological parameters, especially the winds driving the horizontal advection and the characterization of the boundary layer which defines the vertical mixing. Meteorology also affects the chemical lifetime of pollutants.

We use AERMET (EPA, 2019) as a meteorological pre-processor for organizing available data into a format suitable for use by the AERMOD model. AERMET requires both surface and upper air meteorological data, but is designed to run with a minimum of observed meteorological parameters. Vertical profiles of wind speed, wind direction, turbulence, temperature, and temperature gradient are estimated using all available meteorological observations, and extrapolated using similarity (scaling) relationships where needed (EPA, 2018).

Hourly surface data from the nearby Schiphol airport weather station can be obtained from the Integrated Surface Database (ISD, see Smith et al. (2011)). We retrofit observations of temperature, winds, cloud cover, relative humidity, pressure, and precipitation to the SAMSON data format (WebMet, 2019a) which is supported by AERMET. Upper air observations are taken from daily radiosonde observations in De Bilt (at 35 km from Amsterdam), archived in the Integrated Global Radiosonde Archive (IGRA) (Durre et al., 2006). We convert pressure, geopotential height, temperature, relative humidity, dew point temperature, wind speed and direction to the TD6201 data format (WebMet, 2019b) for each reported level up to 300 hPa.

2.3 Air quality measurements

The Public Health Service of Amsterdam (GGD) is the responsible authority for air quality measurements in the Amsterdam area. Within the domain used in this study their NO_2 network consists of 15 reference stations: 5 stations classify as road

station, 5 as urban background station, 2 as industry, 2 as rural, and 1 undecided. Alternatingly, GGD operates a Teledyne API 200E and a Thermo Electron 42I NO/NO$_X$ analyser, both based on chemiluminescence. A catalytic-reactive converter converts NO$_2$ in the sample gas to NO, which, along with the NO present in the sample is reported as NO$_X$. NO$_2$ is calculated as the

190   difference between NO$_X$ and NO. Laboratory calibration estimates the combined uncertainty of hourly NO$_2$ measurement at 3.7% (GGD, 2014).

Low-cost NO$_2$ measurements are taken from the 2016 Urban AirQ campaign (Mijling et al., 2018). Sixteen low-cost air quality sensor devices were built and distributed among volunteers living close to roads with high traffic volume for a 2-month measurement period, from 13 June to 16 August. The devices are built around the NO2-B43F electrochemical cell by

195   Alphasense Ltd (Alphasense, 2018). The sensor generates an electrical current when the target gas diffuses through a membrane where it is chemically reduced at the working electrode. Better sensor performance at low ppb levels is obtained by using low-noise interface electronics. The sensor devices were carefully calibrated in Mijling et al. (2017), solving issues related to sensor drift and temperature dependence. After calibration, they are found to have a typical accuracy of 30%.

3 Calibrating the model

200   Using proxy data instead of real emission introduces the problem to find the emission factors which best relate the activity data to their corresponding emissions. Instead of using theoretical values or values found in literature, we derive effective values which best fit the hourly averaged NO$_2$ observations of a network of N stations.

For a certain hour t, the emission of a source element i belonging to source sector k can be written as

$$E_{ik}(t) = \alpha_k P_{ik}(t) \tag{5}$$

205   in which P_{ki} represent the corresponding emission proxy. The contribution of this source to the concentration at a receptor location j is

$$c_{ijk}(t) = f_{ij}(t)E_{ik}(t) \tag{6}$$

with f_{ij} describing the dispersion of a unit emission from i to j. We apply a regression analysis for a certain period, assuming that for each t the total NO$_2$ concentration c_j at station j can be described as a background field b and a local contribution

210   consisting of a linear combination of the dispersed fields of K emission sectors:

$$c_j(t) = b(t) + \sum_{k=1}^{K} a_k \sum_{i}^{S_k} f_{ij}(t)P_{ik}(t) \tag{7}$$

S_k represents the number of source elements for an emission sector k. The second sum in this equation is calculated for every hour with the Gaussian dispersion model taking the meteorological conditions during t into account. Note that both background concentrations $b(t)$ and local concentrations $c_j(t)$ are observed quantities, see Section 2.2.3 and 2.3. Considering a period of T

215   hours, Eq. (7) can be interpreted as a matrix equation from which the emission factors a_k can be solved using ordinary least squares. Given the physical meaning of a_k, only positive regression results are allowed.

Note that our linearity assumption in Eq. (6) works best when relating NO_X emissions to NO_X concentrations. The non-linearity introduced by the variable NO_2/NO_X ratio (here determined within AERMOD by OLM) is assumed to be sufficiently weak for this assumption to remain valid.

220 In our setup, the emissions are approximated by three sectors highway traffic, urban traffic, and population density (K=3). The resulting a_k do not necessarily represent real emission factors. Their values partly compensate for unaccounted emission sectors and unrealistic modelling (e.g. based on wrong traffic data or an incorrect chemical lifetime). In Retina we update a_k every 24 hours, based on observations of the preceding week (T=168). Doing so, the periodic calibration adjusts itself to seasonal cycles and episodes not captured by the climatologies (e.g. cold spells or holiday periods). To avoid reducing the predictability of the

225 regression model too much (a_k dropping to zero), we do not use all reference stations for calibration, but only stations classified as roadside or urban background. For the Amsterdam network, N=11. The residential emissions are represented by the population density, which is a time invariant proxy. To allow for a diurnal cycle, the residential emission factor is evaluated for two-hour bins. This brings the total number of fitted emission factors to 14: one for highway traffic, one for urban traffic, and 12 describing the daily residential emission cycle.

230 Figure 3 shows an example of the air quality simulation after the emission factors have been determined. The stacked colours in the time series show that the contribution from different emission sectors to local air pollution can strongly vary from site to site.

4 Assimilation of observations

As the air quality network is spatially undersampling the urban area, we need to combine the observations with additional

235 model information to preserve the fine local structures in air pollutant concentrations. From the various geostatistical techniques available we choose Optimal Interpolation (OI) (Daley, 1991), having the desired property that the Bayesian approach allows for assimilation of heterogeneous measurements with different error bars. At an observation location the model value is corrected towards the observation, the innovation depending on the balance between the observation error and the simulation error. The error covariances determine how the simulation in the surroundings of this location is adjusted.

240 Outside the representativity range (i.e. the correlation length) of the observations, the analysis relaxes to the model values.

Consider a state vector $\mathbf{x}$ representing air pollutant concentrations on the (road-following) receptor grid ($n \approx 40{,}000$). Define $\mathbf{x}^b$ as the background, i.e. the model simulation. Observation vector $\mathbf{z}$ contains m measurements, typically 10 – 100. Following the convention by Ide et al. (1997), the OI algorithm can now be written as:

$$\mathbf{x}^a = \mathbf{x}^b + \mathbf{K}(\mathbf{z} - H(\mathbf{x}^b)) \tag{8}$$

245 $$\mathbf{K} = \mathbf{P}^b\mathbf{H}^T(\mathbf{H}\mathbf{P}^b\mathbf{H}^T + \mathbf{R})^{-1} \tag{9}$$

$$\mathbf{P}^a = (\mathbf{I} - \mathbf{K}\mathbf{H})\mathbf{P}^b \tag{10}$$

Matrix $\mathbf{R}$ is the $m \times m$ observation error covariance matrix. As all observations are independent (the measurement errors are uncorrelated), $\mathbf{R}$ is a diagonal matrix with the measurement variances on its diagonal.

$\mathbf{P}^b$ is the $n \times n$ model error covariance matrix, describing how model errors are spatially correlated. The calculation of $\mathbf{P}^b$ is not

250   straightforward; in Section 4.1 an approximation is derived.

Operator H is the forward model, which maps the model state to the observed variables and locations. We can simplify the matrix calculations by reserving the first m elements of the state vector for the observation locations, and the other $n - m$ elements for the road-following grid. The Gaussian dispersion model is evaluated "in-situ" at the observation locations. Avoiding reprojection or interpolation means that there are no representation errors associated with H. The simulations at the

255   observation locations $\mathbf{z}^b$ can then be written as a matrix multiplication

$$\mathbf{z}^b = H(\mathbf{x}^b) = \mathbf{H}\mathbf{x}^b \tag{11}$$

in which $\mathbf{H}$ is an $m \times n$ matrix for which its first m columns form a unity matrix, while its remaining elements are 0.

Eq. (8) describes the analysis $\mathbf{x}^a$, i.e. how the observations $\mathbf{z}$ are combined (assimilated) with the model $\mathbf{x}^b$. It is a balance between the model covariance and the observation covariances, described by the gain matrix $\mathbf{K}$ in Eq. (9). $\mathbf{K}$ determines how

260   strong the analysis must incline towards the observations or remain at the simulated values, to obtain the lowest analysis error variance, $\mathbf{P}^a$ in Eq. (10).

Note that Eq. (8)-(10) are analogous to the first step in Kalman filtering. The second step of the filter, propagating the analysis to the next time step, cannot be made here as the plume model solves a stationary state which is independent of the initial air pollutant concentration field. Also note that since we will use an approximated model error covariance matrix, generally these

265   equations do not lead to an optimal analysis, hence this approach is more correctly referred to as Statistical Interpolation.

Let vector $\mathbf{c}$ represent the observed NO_2 mass concentrations, as described in Section 2.3. The distribution of the air pollutant concentrations resembles better the lognormal distribution than the Gaussian distribution, as can be seen from the Q-Q plots in Fig. 4. The analysis is therefore done in log-space ($z_j = \ln c_j$), which converts lognormal distributions to Gaussian, for which the Bayesian assumptions behind Eq. (8)-(10) are valid. Once returning from the log domain, Eq. (8) can be rewritten as:

270    $$\mathbf{c}^a = \exp(\mathbf{x}^a) = \mathbf{c}^b \exp(\mathbf{K}\Delta\mathbf{z}), \quad \text{with innovation vector } \Delta\mathbf{z} = \mathbf{z} - \mathbf{z}^b \tag{12}$$

By doing the analysis in the log-domain the assimilation updates correspond to multiplication instead of addition: $\exp(\mathbf{K}\Delta\mathbf{z})$ represents the local multiplication factor with which the simulated concentration $\mathbf{c}^b$ is corrected. This means that the shape of the model field (e.g. strong gradients found close to busy roads) is locally preserved. Note that the error in z_j corresponds to the relative error in c_j : $dz = d(\ln c)/dc = dc/c$. The observation error covariance matrix is therefore $\mathbf{R} =$

275    $\text{diag}(\sigma_1^2, \sigma_2^2, \dots, \sigma_m^2)$, with σ_j the relative error corresponding to observation j.

4.1 Modelling the model error covariance matrix

For an optimal result in the data assimilation a realistic representation of the model covariance matrix $\mathbf{P}^b$ is essential. The model covariances influence the spatial representativity of the observations: when model errors correlate over larger distances, the assimilated observation will change the analysis over a longer range. $\mathbf{P}^b$ changes from hour to hour, mainly because varying

280   meteorology changes the atmospheric dispersion properties. We estimate the model error covariance for each hour based on

the spatial coherence of the simulated concentration field. The covariance between two grid locations $\mathbf{x}_i$ and $\mathbf{x}_j$ can be expressed as their correlation ρ and their standard deviations σ:

$$P_{ij}^b \; = \; \sigma_i \, \rho(\mathbf{x}_i, \mathbf{x}_j) \, \sigma_j \tag{13}$$

The model error σ can only be evaluated at locations of the reference network using time series analysis. These model errors
285 are spatially interpolated to other grid locations using IDW, analogous to Eq. (2)-(3). We assume the covariance to be isotropic (i.e. location independent) but inhomogeneous: we parametrize the covariance with a downwind correlation length L_{dw} and a crosswind correlation length L_{cw}. The extend of the correlation lengths reflect the turbulent diffusion and transport of the Gaussian dispersed plumes for a specific hour.

From spatial analysis of the simulation data we see that the correlation depends on distance with a heuristic model

290 $$\rho(d) \; = \exp(-\sqrt{d}) \, , \tag{14}$$

with d the scaled distance between $\mathbf{x}_i$ and $\mathbf{x}_j$ (expressed as x_{dw} and x_{cw} along the downwind and crosswind axes)

$$d = \sqrt{\left(\frac{x_{\text{dw}}}{L_{\text{dw}}}\right)^2 + \left(\frac{x_{\text{cw}}}{L_{\text{dw}}}\right)^2} \, , \tag{15}$$

such that all points on an ellipse with semi-major axis L_{dw} and semi-minor axis L_{cw} have the same correlations.

To fit the parameters L_{dw} and L_{cw} for a certain hour, we select 1000 sample locations from the road-following grid. To represent
295 both polluted and less polluted areas, the locations are selected such that their concentrations are homogeneously distributed over the value range, excluding the first and last 5 percentile. For this sample, correlation lengths L_{dw} and L_{cw} are fitted using Eq. (14) and (15).

Figure 5 shows the results of this analysis for two different hours. For fields with low gradients (e.g. when traffic contribution is low at night), large values of L can occur. To prevent assimilation instabilities, the fitted values of L are limited to a maximum
300 of 10 km. During the 2016 summer months, longest correlation lengths are found for fields with low gradients. Average midnight values, when traffic contribution is low, are about 8 km. Correlation lengths are shortest during the morning rush hour (~1 km), increasing to 3 km during the late morning and afternoon. There is a wind dependency, as stronger winds stretch the pollution plumes, increasing correlation lengths. From the fit results we find an average ratio between L_{cw} and L_{dw} of 68%. Once the covariance parameters are known, the covariance matrix elements are calculated with Eq. (13). Note that for the
305 calculation of the gain matrix $\mathbf{K}$ there is no need to calculate the full $\mathbf{P}^b$ matrix. Instead we calculate $\mathbf{P}^b\mathbf{H}^{\mathrm{T}}$, which due to the structure of $\mathbf{H}$ this matrix product corresponds to the first m columns of the $n{\times}n$ matrix $\mathbf{P}^b$.

5 Validation of simulation and assimilation

We validate the system for the period June 15 - August 15 in 2016 with hourly observations from station NL49019 (Oude Schans), located in the city centre and classified as an urban background site. We test (1) the ability to simulate the NO_2
310 concentrations at this location with the dispersion model, and (2) the effectiveness of the data assimilation when only measurements of the neighbouring reference stations are included in the assimilation (i.e. a leave-one-out approach). From the

results in Fig. 6 we see that the simulation describes the hourly observations with an RMSE of 11.7 μg/m³. The results improve considerably when the surrounding observations of the reference network are assimilated, taking advantage of the covariance between the observational information from nearby stations and the validation location. The error reduces to 7.6 μg/m³, while

315 the correlation improves from 0.52 to 0.82.

To assess the data quality across the domain, we perform a leave-one-out analysis at all locations of the reference network for the period June 1 - August 31, 2016. The results are summarized in Table 3. For the observation-free simulation (i.e. the model forecast) we find an average RMSE of 13.6 μg/m³ and correlation of 0.57. When assimilating observations, the average RMSE drops to 10.4 μg/m³ while the correlation increases to 0.78. Strong systematic underestimations of the simulation (characterized

320 by a large negative bias) are observed at street locations NL49002, NL49007 and industrial locations NL49546, NL49704. These are most likely caused by unrealistic assumptions of local emissions of either traffic or industry. The strong positive bias found at NL49014, located in a city park separated from the nearby main road by a block of 4-storey buildings, might be explained by an incorrect simulation of air pollutants in the direct vicinity of these buildings.

The CAMS regional ensemble analysis compares well with the average of the urban background stations; the very low bias (-

325 0.1 μg/m³) corresponds with the fact that data of these stations are used in its analysis. (Note that we use here the CAMS values corresponding to the Amsterdam grid cell, not the 3x3 minimum values used as background for the modelling.) On the other hand, it shows strong underestimations at street locations, as expected. It is here where the Retina simulation outperforms the low resolution results of CAMS.

From Table 3 we can see that the relative error in the model forecast (defined as the ratio between the RMSE and the mean of

330 the observations) is around 58% on average. When assimilating, the error becomes dependent on the distance to the nearest observation locations. For sites having the nearest assimilated observation within 2 km distance, the average RMSE drops from 16.8 to 11.9 μg/m³, corresponding to an average relative error of 39%. For sites where the nearest assimilated observation is further away than 2 km, the average RMSE drops from 10.8 to 9.1 μg/m³, corresponding to an average relative error of 53%.

6 Added value of low costs sensors

335 The previous analysis is purely based on high-quality reference measurements. In this section we explore whether the statistical interpolation scheme can be used to derive useful information of low-cost measurements, despite their larger inaccuracy.

During the Urban AirQ campaign (see Section 2.3) sensor SD04 was mounted at 120 m distance from location NL49019. From the hourly time series in Fig. 6 it can be seen that including its sensor data in the assimilation leads to a better description of NO₂ concentrations at location NL49019 than when assimilating with reference data alone. The RMSE drops from 7.6

340 μg/m³ to 4.7 μg/m³, while the correlation improves from 0.82 to 0.92.

Next, we use all reference data and all low-cost sensor data from the first half of the Urban AirQ campaign to construct a monthly averaged concentration map of Amsterdam, see Fig. 7. The addition of the low-cost data lowers the assimilation results by several μg/m³ in the undersampled area west of Oude Schans, while the NO₂ increases with several μg/m³ around

the traffic arteries found south and east of this location. A large fraction of traffic on these roads uses the IJ-tunnel to cross the
345   river. On a monthly basis, this tunnel is used by approximately one million vehicles.

The second half of the Urban AirQ campaign coincides with the start of the summer holiday period and the closure of the IJ-tunnel for maintenance. Comparison of the NO_2 concentration maps of both periods reveal interesting features (Fig. 8). Overall, the NO_2 concentrations drop around 10% due to reduced traffic during the summer break. Notable exception is the historic city center, where the NO_2 reduction is only a few percent, probably related to the steady economic activity driven by tourism.
350   The strongest NO_2 reductions, around 15%, are found around the access ways of the IJ-tunnel. A few main roads (e.g. De Ruijterkade/Piet Heinkade and Ceintuurbaan) show less NO_2 reduction than average, apparently due to redirected traffic avoiding the tunnel.

7 Discussion

The validation analysis in Section 5 confirms that the CAMS ensemble is a good predictor for hourly NO_2 concentrations
355   found in the urban background. However, local effects can be better resolved when CAMS data is used for background concentrations in a dispersion model which is driven by proxies for traffic and residential emissions.

The Retina simulation setup shows that such a system can be built from open software and open data. Applied to Summer 2016 in Amsterdam, it reduces the relative error at street locations from 70% to 51%, mainly by reducing the negative bias from 18.2 to 5.3 $\mu g/m^3$. At urban background locations the dispersion model introduces often a positive bias, especially when
360   traffic sources are nearby. This is probably related to the assumption of uniform surface roughness used by the dispersion model to account for the urban structure. A better description of street canyons in the model is likely to reduce this bias. Also unrealistic assumptions about chemical lifetime of NO_2 (influencing the plume "length") might play a role here.

The Retina approach works best for areas where air pollution is dominated by transport and residential emissions. Significant inaccuracies will be found in areas dominated by local emissions (e.g. from industry, port and airport activity) which are not
365   described adequately by the proxies. This can be addressed by including these sources explicitly in the dispersion modelling.

The mapping results improve considerably with the second Retina step when available observations are assimilated by the statistical interpolation scheme. In general, the error of the assimilation results depends on the accuracy of air quality model, the number of assimilated observations, the quality of observations, and the distance to the observation location. When assimilating measurements of the reference network, the relative error in NO_2 concentrations drop to 44% on average. The
370   local error depends on the distance to the nearest observations: approximately 39% within 2 km of an observation site, increasing to 53% for larger distances. The typical correlation increases from 0.6 to 0.8.

Retina has been built on open data to facilitate a flexible application to other cities. The meteorology needed for AERMOD is taken from global data sets of ISD and IGRA. Road network information can also be obtained globally from OpenStreetMap. Traffic data tend to be harder to obtain. When no local data is available on diurnal and weekly traffic flow its patterns should
375   be estimated. In the absence of local census data, population density data can be taken from the Global Human Settlement

database (Schiavina et al., 2019), which has global coverage on a 250 m resolution. For application within Europe, the necessary background pollutant concentrations can be obtained from CAMS. For applications outside Europe other data sets have to be found.

For near-real time monitoring and forecasting of air quality the CAMS ensemble analysis must be changed for the ensemble
380 forecast. Instead of observation-based meteorology one should use data from local or global numerical weather prediction models e.g. from the National Centers for Environmental Prediction (the Global Forecast System, GFS; open data) or the European Centre for Medium-Range Weather Forecasts (ECMWF; not open data).

8 Conclusions

In this paper we have presented Retina, a practical approach to interpolating hourly urban air quality measurements. As air
385 pollution gradients can be strong in the urban environment, it is essential to combine (sparse) measurements with an air quality model when aiming at street-level resolution. The first step of Retina consists of a simulation by a dispersion model which is driven by meteorological data and proxies for traffic and residential emissions. In the second step, observations of different accuracy are assimilated using a statistical interpolation scheme.

A reasonable approximation of the model covariance matrix is found by assuming the model covariance to be isotropic and by
390 fitting correlation lengths along the downwind and crosswind axes for every hour. Finding a more realistic description of the model covariance matrix may further improve the assimilation results, which will be subject of future research.

Retina can be used for an enhanced understanding of reference measurements by deriving detailed observation-based concentration maps. The Bayesian assimilation scheme also allows us to improve the results by including low-cost sensor data, in order to get improved localized information. However, biases must be removed beforehand with careful calibration, as most
395 low-cost air quality sensors suffer from issues like cross-sensitivity or signal drift, see e.g. Mijling et al. (2018).

The assimilation of low-cost sensor data from the Urban AirQ campaign reveals more detailed structure in concentration patterns in an area which is undersampled by the official network. The additional measurements correct for wrong assumptions in traffic emissions used in the apriori interpolation, and give better insight in how traffic rerouting (for instance due to closure of an arterial road) affects local air quality.

400 Apart from assessment of historic data such as in this study, Retina has been applied successfully for near-real time monitoring and forecasting of NO_2 in the cities of Amsterdam, Barcelona, and Madrid. Future work includes the application of Retina to other cities inside and outside of Europe, and the application of Retina to other pollutants such as particulate matter.

Author contribution

405   All work in this study was carried out by the author.

Competing interests

The author declares that he has no conflict of interest.

Acknowledgements

The author wishes to acknowledge the people behind the data sources used in this study, most notably GGD Amsterdam
410   (reference measurements), volunteers of the Urban AirQ campaign (low-cost measurements), NDW and Amsterdam Traffic
Research Department (traffic data), contributors to OpenStreetMaps (road location and classification), CAMS (background
concentrations), IGRA and ISD (meteorology), and CBS (population data). This research was supported by KNMI-DataLab
and the EU-H2020 project AirQast.

References

415   Alphasense: Alphasense Data Sheet for NO2-B43F, April 2016, available at: http://www.alphasense.com/WEB1213/wp-
content/uploads/2018/12/NO2B43F.pdf (last access: 1 September 2019), 2018.

Beelen, R., Hoek, G., Vienneau, D., Eeftens, M., Dimakopoulou, K., Pedeli, X., Tsai, M.-Y., Künzli, V, Schikowski, T.,
Marcon, A., Eriksen, K. T., Raaschou-Nielsen, O., Stephanou, Eu., Patelarou, E., Lanki, T., Yli-Tuomi, T., Declercq, Ch.,
Falq, G, Stempfelet, M., Birk, M., Cyrys, J., von Klot, S., Nádor, G., Varró, M. J., Dėdelė, A., Gražulevičienė, R., Mölter, A.,
420   Lindley, S., Madsen, Ch., Cesaroni, G., Ranzi, A., Badaloni, Ch., Hoffmann, B., Nonnemacher, M., Krämer, U., Kuhlbusch,
T., Cirach, M., de Nazelle, A., Nieuwenhuijsen, M., Bellander, T., Korek, M., Olsson, D., Strömgren, M., Dons, E., Jerrett,
M., Fischer, P., Wang, M., Brunekreef, B., and de Hoogh, K.: Development of NO_2 and NO_X land use regression models for
estimating air pollution exposure in 36 study areas in Europe – The ESCAPE project, Atmospheric Environment, Volume 72,
2013, Pages 10-23, ISSN 1352-2310, doi:10.1016/j.atmosenv.2013.02.037, 2013.
425   CAMS: Copernicus Atmosphere Monitoring System, European-scale air quality analysis from model ensemble,
https://atmosphere.copernicus.eu/data, last access: 25 October 2019, 2019.

CBS: Statistics Netherlands, Statistische gegevens per vierkant 2000-2014, https://www.cbs.nl/nl-nl/dossier/nederland-
regionaal/gemeente/ruimtelijke-statistieken, last access: 25 October 2019, 2016.

Cimorelli, A.J., S.G. Perry, A. Venkatram, J.C. Weil, R.J. Paine, R.B. Wilson, R.F. Lee, W.D. Peters, and R.W. Brode:

430   AERMOD: A dispersion model for industrial source applications Part I: General model formulation and boundary layer characterization, J.Appl.Meteor. 44, 682-693, 2004.

Daley, R.: Atmospheric Data Analysis. Cambridge University Press, 1991.

Denby, B.R.: Mapping of NO_2 concentrations in Bergen (2012-2014). METreport No. 12/15, Norwegian Meteorological Institute, ISSN 2387-4201, 2015.

435   Durre, I., Vose, R. S., and Wuertz, D. B.: Overview of the Integrated Global Radiosonde Archive. Journal of Climate, 19, 53-68, 2006.

EPA: Technical support document (TSD) for NO_2-related AERMOD modifications, U.S. Environmental Protection Agency, EPA-454/B-15-004, July 2015, 2015.

EPA: AERMOD Model Formulation and Evaluation, EPA-454/R-18-003, April 2018, available at

440   https://www3.epa.gov/ttn/scram/models/aermod/aermod_mfed.pdf, 2018.

EPA: User's Guide for the AERMOD Meteorological Preprocessor (AERMET), EPA-454/B-19-028, August 2019, available at https://www3.epa.gov/ttn/scram/7thconf/aermod/aermet_userguide.pdf, 2019.

GGD: Foutenbeschouwing (revisie) kalibratie van eerstelijns standard (In Dutch), Public Health Service of Amsterdam (GGD), GGD/LO 14-1134, July 2014, 2014.

445   Harrison, R. M.: Urban atmospheric chemistry: a very special case for study, Nature, npj Climate and Atmospheric Science, 20175, 2397-3722, doi:10.1038/s41612-017-0010-8, 2018.

Ide, K., Courtier, P., Ghil, M., and Lorenc, A. C.: Unified notation for data assimilation: Operational, sequential and variational. J. Met. Soc. Japan,75, 181–189, 1997.

IGRA: National Oceanic and Atmospheric Administration, Integrated Global Radiosonde Archive, version 2.

450   https://www.ncdc.noaa.gov/data-access/weather-balloon/integrated-global-radiosonde-archive, last access: 25 October 2019, 2019.

ISD: National Oceanic and Atmospheric Administration, Integrated Surface Database, https://www.ncdc.noaa.gov/isd/data-access, last access: 25 October 2019, 2019.

Janssens-Maenhout, G., Pagliari, V., Guizzardi, D., and Muntean, M.: Global emission inventories in the Emission Database

455   for Global Atmospheric Research (EDGAR) - Manual (I): Gridding: EDGAR emissions distribution on global gridmaps, JRC Technical Reports, 33 pp., doi:10.2788/81454, 2013.

Lefebvre, W., Fierens, F., Trimpeneers, E., Janssen, S., Van de Vel, K., Deutsch, F., Viaene, P., Vankerkom, J., Dumont, G. , Vanpoucke, C., Mensink, C., Peelaerts, W., and Vliegen, J.: Modeling the effects of a speed limit reduction on traffic-related elemental carbon (EC) concentrations and population exposure to EC, Atmos. Env., 45, pp. 197-207,

460   doi:10.1016/j.atmosenv.2010.09.026, 2011.

Lelieveld J., Haines, A., and Pozzer, A.: Age-dependent health risk from ambient air pollution: a modelling and data analysis of childhood mortality in middle-income and low-income countries. Lancet Planet Health 2018; 2(7): e292-e300, 2018.

Liu, F., Beirle, S., Zhang, Q., Dörner, S., He, K., and Wagner, T.: NO_X lifetimes and emissions of cities and power plants in polluted background estimated by satellite observations, Atmos. Chem. Phys., 16, 5283–5298, doi:10.5194/acp-16-5283-2016, 2016.

Makido, Y., Dhakal, S., and Yamagata, Y.: Relationship between urban form and CO2 emissions: Evidence from fifty Japanese cities, Urban Climate, 2, pp. 55-67, doi:10.1016/j.uclim.2012.10.006, 2012.

Maréclal, V., Peuch, V.-H., Andersson, C., Andersson, S., Arteta, J., Beekmann, M., Benedictow, A., Bergström, R., Bessagnet, B., Cansado, A., Chéroux, F., Colette, A., Coman, A., Curier, R. L., Denier van der Gon, H. A. C., Drouin, A., Elbern, H., Emili, E., Engelen, R. J., Eskes, H. J., Foret, G., Friese, E., Gauss, M., Giannaros, C., Guth, J., Joly, M., Jaumouillé, E., Josse, B., Kadygrov, N., Kaiser, J. W., Krajsek, K., Kuenen, J., Kumar, U., Liora, N., Lopez, E., Malherbe, L., Martinez, I., Melas, D., Meleux, F., Menut, L., Moinat, P., Morales, T., Parmentier, J., Piacentini, A., Plu, M., Poupkou, A., Queguiner, S., Robertson, L., Rouïl, L., Schaap, M., Segers, A., Sofiev, M., Tarasson, L., Thomas, M., Timmermans, R., Valdebenito, Á., van Velthoven, P., van Versendaal, R., Vira, J., and Ung, A.: A regional air quality forecasting system over Europe: the MACC-II daily ensemble production, Geosci. Model Dev., 8, 2777–2813, doi:10.5194/gmd-8-2777-2015, 2015.

Mijling, B., Jiang, Q., de Jonge, D., and Bocconi, S.: Field calibration of electrochemical NO_2 sensors in a citizen science context, Atmos. Meas. Tech., 11, 1297-1312, doi:10.5194/amt-11-1297-2018, 2018.

NDW: National Data Warehouse for Traffic Information, Historical data https://www.ndw.nu/pagina/en/78/database, last access: 25 October 2019, 2019.

OSM: OpenStreetMap contributors, Planet dump retrieved from https://planet.osm.org. https://www.openstreetmap.org, 2017.

Schneider, P., Castell, N., Vogt, M., Dauge, F. R., Lahoz,, W. A., and Bartonova, A.: Mapping urban air quality in near real-time using observations from low-cost sensors and model information, Environment International, 106, 234-247, doi:10.1016/j.envint.2017.05.005, 2017.

Schneider, P., Bartonova, A., Castell, N., Dauge, F. R., Gerboles, M., Hagler, G. S. W., Hüglin, Ch., Jones, R. L., Khan, S., Lewis, A. C., Mijling, B., Müller, M., Penza, M., Spinelle, L., Stacey, B., Vogt, M., Wesseling, J., and Williams, R. W.: Toward a Unified Terminology of Processing Levels for Low-Cost Air-Quality Sensors, Environmental Science & Technology 2019 53 (15), 8485-8487, DOI: 10.1021/acs.est.9b03950, 2019.

Schiavina, M., Freire, S., and MacManus, K.: GHS population grid multitemporal (1975, 1990, 2000, 2015) R2019A. European Commission, Joint Research Centre (JRC), doi:10.2905/42E8BE89-54FF-464E-BE7B-BF9E64DA5218, 2019.

Smith, A., Lott, N., and Vose, R.: The Integrated Surface Database: Recent Developments and Partnerships. Bulletin of the American Meteorological Society, 92, 704–708, doi:10.1175/2011BAMS3015.1, 2011.

Sokhi, R. S., Middleton, D. R., Luhana, L.: Review of methods for NO to NO_2 conversion in plumes at short ranges. Science Report: SC030171/SR2. Environment Agency, Bristol, United Kingdom, 2007.

WebMET: SAMSON Surface Met Data, http://www.webmet.com/MetGuide/Samson.html, last access: 25 October 2019, 2019a.

WebMET: TD6201 - Upper Air Data for AERMOD, http://www.webmet.com/MetGuide/TD6200.html, last access: 25 October 2019, 2019b

WHO: Global Urban Ambient Air Pollution Database (update 2016). World Health Organization, https://www.who.int/airpollution/data/cities-2016/en/, last access: 25 October 2019, 2016.

500   WMO: Low-cost sensors for the measurement of atmospheric composition: overview of topic and future applications, WMO-No. 1215, A. C. Lewis, E. Schneidemesser, and R. E. Peltier, Eds., World Meteorological Organization, 2018.
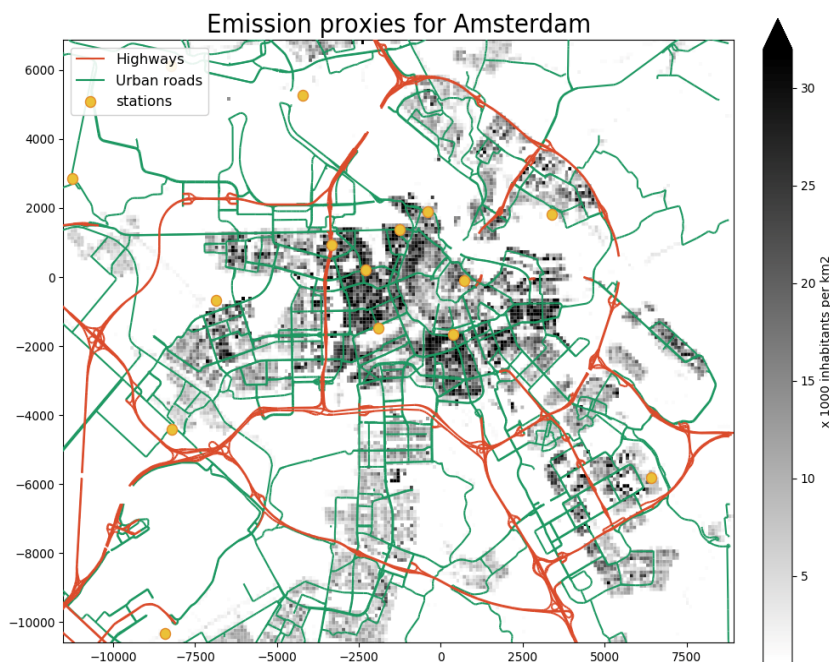
Figure 1: Map of the emission proxies used for the dispersion model. Red lines indicate the highways, green lines indicate the urban main roads. Grey colours indicate the population density. The locations of the reference measurement sites are indicated with the yellow dots. Units on the axes are in meters. (Road location data adopted from © OpenStreetMap contributors 2019. Distributed under a Creative Commons BY-SA License.)
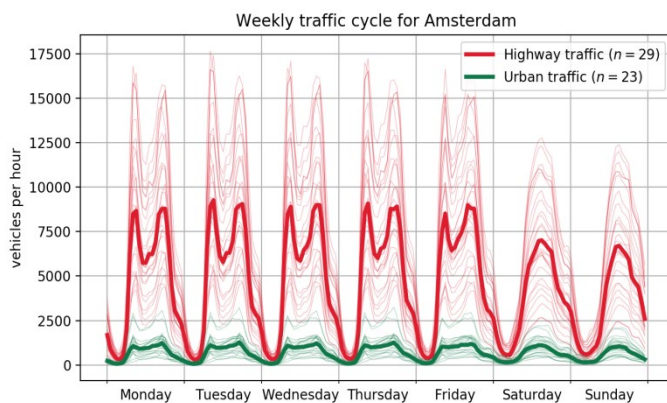
Figure 2: Weekly cycle of highways in the Amsterdam area, as opposed to the weekly cycle of urban roads. The morning and evening rush hours on working days are clearly visible for highways. Urban traffic has, apart from lower volume, less distinct peaks. The thick lines show the median of traffic flow for both road types.
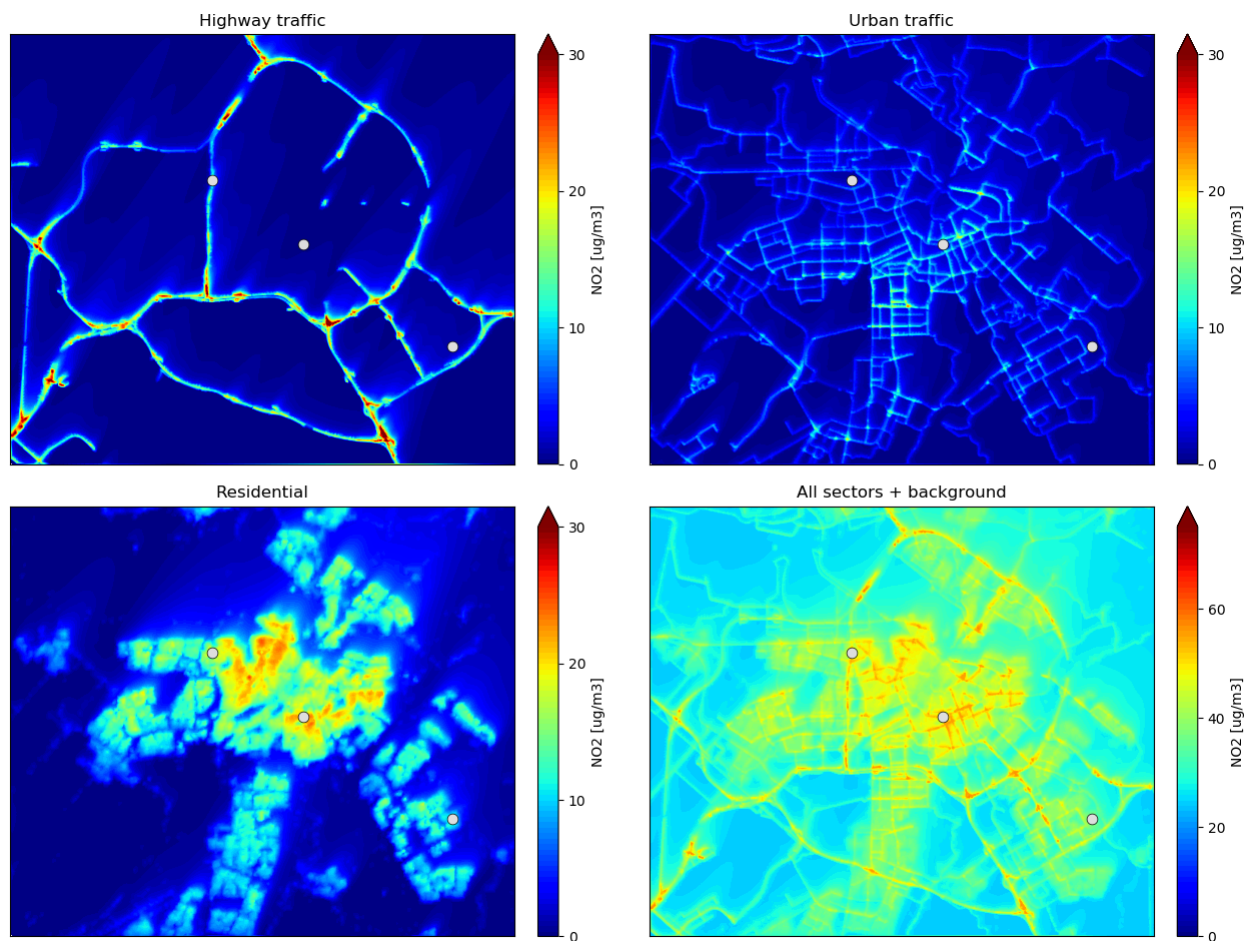
Figure 3a: Dispersion maps of NO₂ concentrations for each emission sector at 8 July 2016, 9:00. The lower right panel shows the linear combination which best fits the time series at the calibration sites. Wind is blowing from the southwest at 16 km/h.
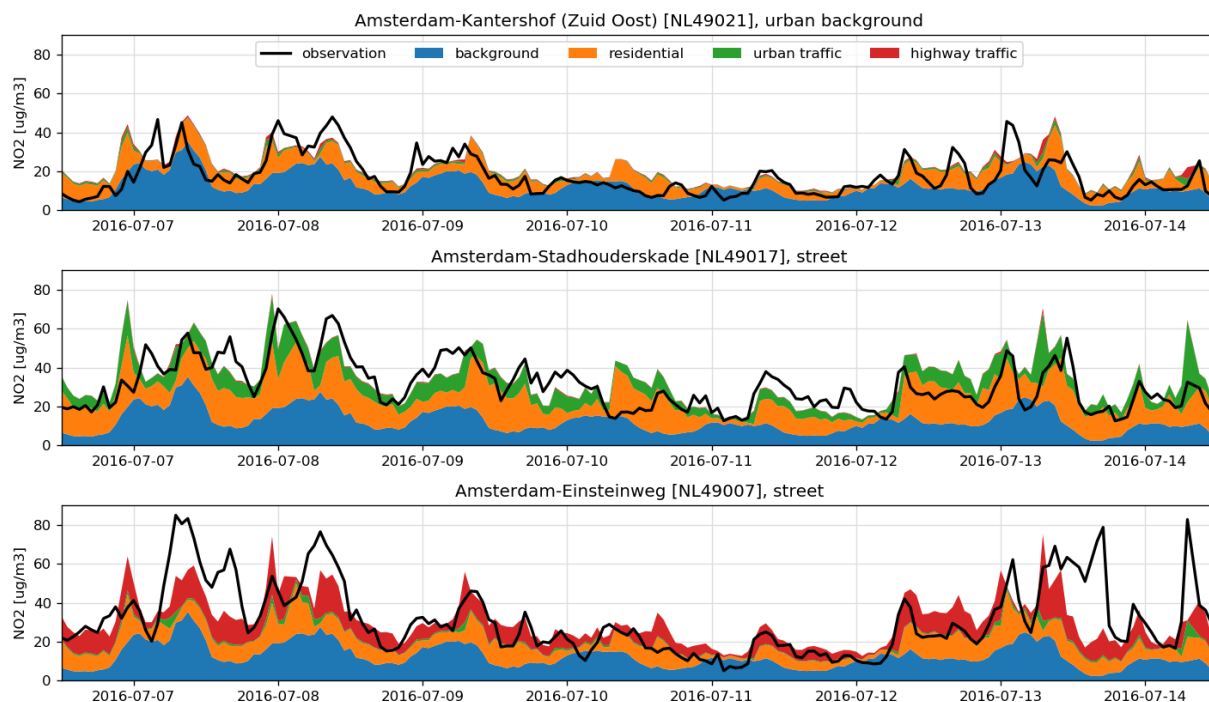
515

Figure 3b: Comparison of observed and simulated NO₂ time series for three different sites (marked with grey dots above): an urban background location, a street location, and a highway location. The colours indicate the simulated contribution of the three source sectors and the background.
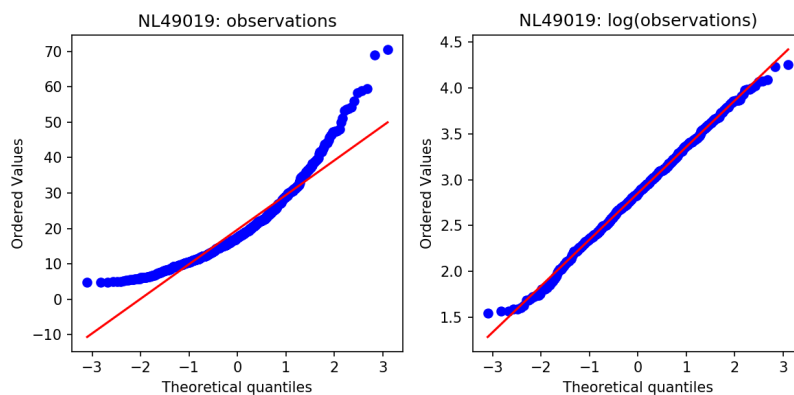
520

Figure 4: (left) Distribution of the NO₂ observations at reference station Oude Schans in July 2016 compared to a standard normal distribution. (right) The logarithm of the observed values correspond better to a Gaussian distribution, shown by the quantile value pairs being almost on a straight line.

525
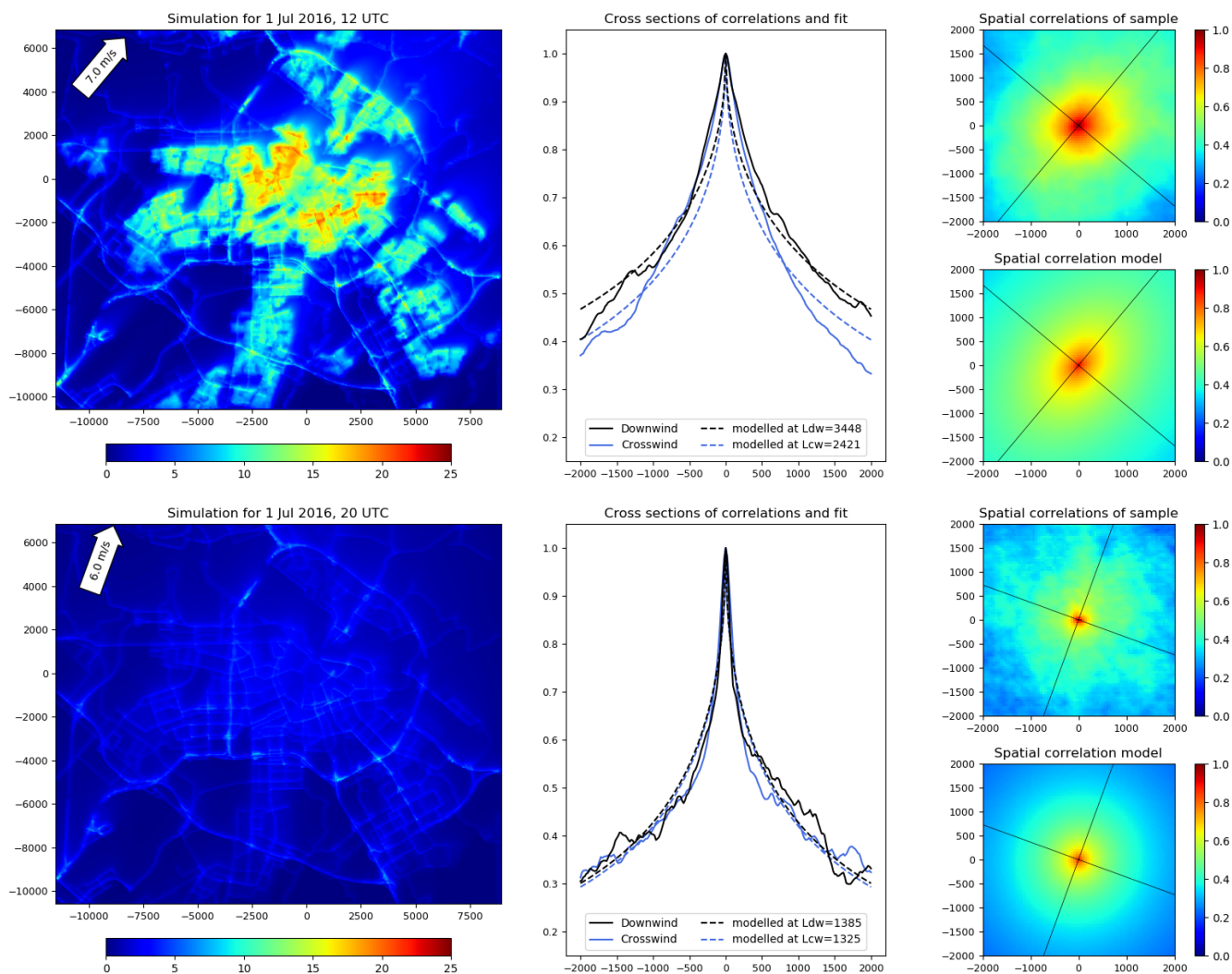
Figure 5: Simulated NO₂ concentration fields at two different hours. The middle panels show the correlations along the downwind and crosswind axes. The right panels show and the spatial correlations of a sample (n=1000) and the resulting modeled spatial correlation model. Units are in meters.
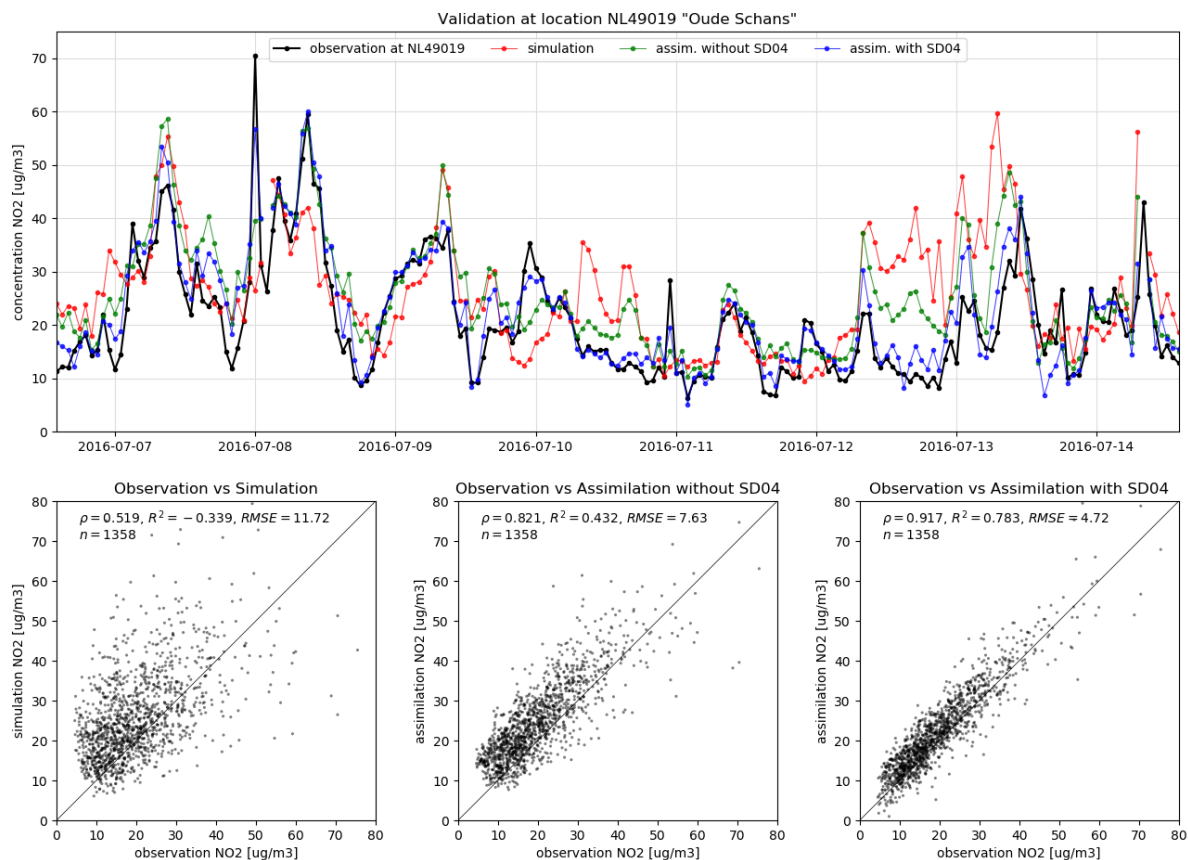
530

Figure 6: (top) 8-day snapshot of NO₂ time series of observation, simulation, and assimilation at location "Oude Schans". Assimilation is performed with data from reference stations alone (green line), and with additional data from nearby low-cost sensor SD04 (blue line). (bottom) Scatter plots of observation against simulation and assimilation for the June 15 -August 15 2016 period. Statistics of the *n* data pairs are given in correlation (ρ), coefficient of determination (R^2), and RMSE.

535
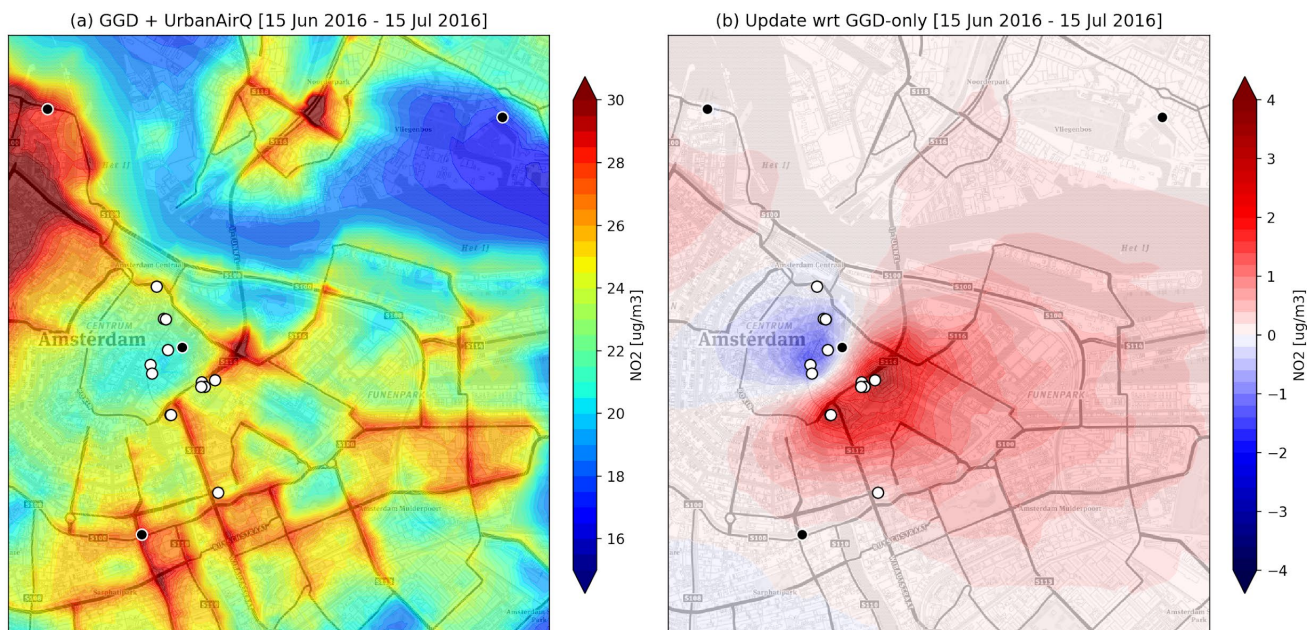
Figure 7: (a) 30-day average of NO₂ concentrations in the center of Amsterdam, after assimilation of both reference measurements (black dots) and low-cost measurements (white dots). (b) Changes in spatial pattern when low-cost measurements are included in the analysis. (Basemap source: © Mapbox © OpenStreetMap contributors 2019. Distributed under a Creative Commons BY-SA License.)

540
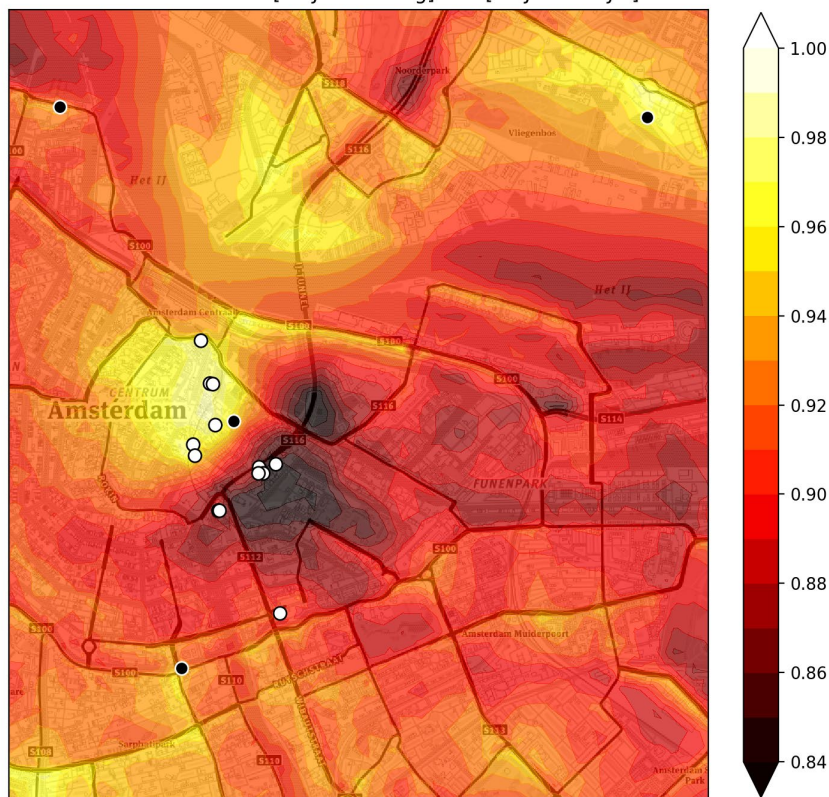
Figure 8: Reduction of NO₂ during the holiday period. Largest reduction of concentrations is found in the vicinity of access ways to the IJ-tunnel, which was closed for maintenance. Concentrations in the historic center remain unchanged. (Basemap source: © Mapbox © OpenStreetMap contributors 2019. Distributed under a Creative Commons BY-SA License.)

545

Table 1: Overview of AERMOD simulation settings

Road width	20 m
Emission height traffic	0.5 m
Emission height residential	10 m
Initial vertical extension of concentration layer (sigma Z_0)	10 m
Receptor grid	Road following
Receptor height	1.5 m
Urban surface roughness length	1 m
NO_2/NO_X ratio	Ozone Limited Method (OLM), Primary emission ratio 10%
NO_X lifetime	2 h
Other AERMOD modelling options	Optimizing model runtime for sources (FASTALL) Address low wind speed conditions (LOWWIND3) Assuming flat terrain (FLAT)

550 **Table 2: Summary of simulation input data for Amsterdam**

Emission	Highway locations	OpenStreetMap (OSM, 2017): street segments labelled motorway and trunk
	Urban road locations	OpenStreetMap (OSM, 2017): street segments labelled primary, secondary, tertiary
	Highway traffic flow	National Data Warehouse for Traffic Information (NDW, 2019): weekly cycle of vehicle counts at 29 selected locations (2016), interpolated to street segments
	Urban traffic flow	Amsterdam municipality (personal communication): weekly cycle of vehicle counts at 24 locations (2016), interpolated to street segments
	Population data	Statistics Netherlands (CBS, 2016): population density (2014) gridded at 100 m resolution
Observation	Background NO_2	Copernicus Atmosphere Monitoring Service (CAMS, 2019): NO_2 analysis from model ensemble; minimum value found in 3x3 grid around domain center
	Background O_3	Copernicus Atmosphere Monitoring Service (CAMS, 2019): O_3 analysis from model ensemble; mean value found in 3x3 grid around domain center
Meteorology	Meteorology (surface)	Integrated Surface Database (ISD, 2019): hourly observations from Schiphol Airport weather station
	Meteorology (upper air)	Integrated Global Radiosonde Archive (IGRA, 2019): daily radio sounding at De Bilt (NL)

Table 3: Validation results at reference locations, June-August 2016

				mean	CAMS ensemble			Model forecast			Assimilated observations			
ID	name	type	n[1]	obs.	RMSE[2]	bias	corr	RMSE[2]	bias	corr	RMSE[2]	bias	corr	dist[3]
NL49002	Amsterdam - Haarlemmerweg	street	2145	42.2	31.4	-25.6	0.49	22.6	-14.3	0.55	18.6	-14.5	0.83	0.99
NL49007	Amsterdam - Einsteinweg	street	2145	38.1	29.2	-21.4	0.42	19.6	-6.9	0.57	16.5	-6.2	0.72	1.26
NL49012	Amsterdam - Van Diemenstr.	street	2145	29.1	20.2	-12.5	0.53	15.7	-2.7	0.57	9.7	-0.5	0.87	0.99
NL49017	Amsterdam - Stadhouderskade	street	2140	30.1	17.9	-13.5	0.45	14.3	1.9	0.50	9.0	-2.7	0.78	1.60
NL49020	Amsterdam - Jan van Galenstraat	street	2131	34.8	24.0	-18.2	0.59	16.6	-4.7	0.58	11.1	-5.3	0.86	1.26
NL49003	Amsterdam - Nieuwend. dijk	urban backgr.	2145	16.6	8.6	0.1	0.60	10.5	2.0	0.47	7.5	0.8	0.71	3.28
NL49014	Amsterdam - Vondelpark	urban backgr.	2115	17.3	9.0	-0.7	0.52	14.9	7.9	0.44	9.9	6.5	0.75	1.73
NL49019	Amsterdam - Oude Schans	urban backgr.	2124	20.7	10.3	-4.1	0.59	13.8	5.8	0.50	8.7	4.6	0.81	1.60
NL49021	Amsterdam - Kantershof	urban backgr.	2082	14.9	7.5	1.6	0.65	10.7	5.6	0.56	8.0	4.4	0.73	7.33
NL49022	Amsterdam - Sportp. Ookmeer	urban backgr.	2124	14.3	8.4	2.4	0.65	9.2	3.4	0.66	8.0	3.7	0.80	3.89
NL49565	Oude Meer - Aalsmeerderdijk	rural	2127	17.3	9.1	-0.6	0.57	9.0	-2.4	0.59	8.0	-3.0	0.73	5.94
NL49703	Amsterdam - Spaarnwoude	rural	2125	13.0	8.7	3.7	0.61	8.1	2.1	0.60	7.5	2.4	0.71	4.47
NL49546	Zaanstad - Hemkade	industry	2145	22.9	14.3	-6.2	0.63	15.0	-8.1	0.66	13.0	-8.3	0.83	3.26
NL49704	Zaanstad - Hoogtij	industry	2120	19.6	12.7	-3.0	0.66	13.4	-6.0	0.72	12.1	-6.4	0.84	3.72
NL49561	Badhoevedorp - Sloterweg	undecided	2145	20.5	10.6	-3.9	0.64	10.8	-2.9	0.61	8.9	-4.2	0.79	3.96
Average street locations				**34.9**	**24.5**	**-18.2**	**0.50**	**17.8**	**-5.3**	**0.55**	**13.0**	**-5.8**	**0.81**	

Average urban background locations	16.8	8.8	-0.1	0.60	11.8	4.9	0.53	8.4	4.0	0.76	
Average all locations	23.4	14.8	-6.8	0.57	13.6	-1.3	0.57	10.4	-1.9	0.78	

555   1)   Number of samples
2)   In units µg/m^3
3)   The distance to the nearest observation site, in km